

PAPER PROPOSED FOR IFAR SESSION

PREDICTION OF STRUCTURAL VIBRATIONS INDUCED BY MASS-UNBALANCED ELECTRIC PROPULSION SYSTEMS

Gabriel R. Dias, Dante V. Rocha e Silva, Allan G. Heck & Domingos A. Rade

Mechanical Engineering Division, Aeronautics Institute of Technology, São José dos Campos - Brazil

Abstract

Distributed electric propulsion can introduce new dynamic interactions between flexible aircraft structures and motor-propeller assemblies. In particular, mass unbalance in multiple rotating propellers may generate persistent harmonic loads and induce high vibration levels in lightweight flexible wings. This work investigates the structural and aeroelastic vibration response of a flexible wing equipped with two electric motor-propeller assemblies simultaneously subjected to mass-unbalance excitation. A three-dimensional finite-element structural model is developed, including bending and torsional deformations of the wing, pitch and yaw rotations of the propellers, and thrust loads. In addition, vertical offsets between the wing elastic axis and the propeller axis are introduced to better represent the geometry of pylons found in actual aircraft. The aerodynamic loads are represented using Theodorsen's unsteady thin-airfoil theory converted to the time domain through Wagner's approximation. Numerical simulations are performed to evaluate the influence of some relevant parameters related to the unbalance load and pylon geometry. The results show that rotation speed mismatch induces significant beating patterns in the vibration responses, while aerodynamic coupling significantly modifies both the transient and steady-state responses. In addition, the phase difference between the unbalance forces and the vertical offset of the propeller axis are shown to significantly affect the vibration levels. Campbell diagrams are also presented to characterize the dynamics of the coupled system.

Keywords: aircraft vibrations, electric propulsion, unbalance, rotating machines, structural dynamics

1. Introduction

In response to current environmental-related emission targets and the long-term goal of net-zero emissions, the aerospace industry has been investigating alternative propulsion architectures, including distributed electric propulsion (DEP) concepts [1].

DEP usually replaces a small number of large conventional engines with multiple smaller electric motors distributed along the airframe, usually along the wing span. This arrangement may improve propulsive efficiency, reduce noise, and provide aerodynamic benefits due to the interaction between the propeller slipstream and the wing [2]. However, the installation of several motor-propeller assemblies modifies the structural layout, mass distribution, inertial properties, and loading conditions of the aircraft. As a result, the dynamic and aeroelastic behavior of DEP configurations may differ significantly from that of conventional aircraft.

Several studies have investigated the influence of distributed propulsion on aeroelastic stability. Xu [3] analyzed propeller-wing whirl flutter mechanisms, while Böhnisch et al. [4] studied the effect of the number and position of propulsors on the stability of flexible wings. Other works have also addressed the influence of distributed electric propulsors on flutter boundaries [5, 6, 7].

https://doi.org/10.71945/icas2026$_0$901

In addition, other factors affect the dynamic characteristics of DEP aircraft, especially thrust loads and mass unbalance. Thrust acts by following the bending and torsional deformations of the wing, thus altering [8, 9, 10]. On the other hand, any unbalance in the propellers, either caused by manufacturing imperfections or by degradation over time, induces continuous vibrations in the structure. Mirabbashi et al. [11] and Zafari et al. [12] studied how unbalanced engines affect the aircraft, showing that they can cause resonant vibration and worsen flutter conditions.
In this context, the present work investigates the structural vibration response of a flexible wing equipped with two electric motor-propeller assemblies subjected to mass-unbalance excitation. A three-dimensional finite-element structural model is developed, intended for the prediction of the coupled vibrational behavior of the mechanical wing-propulsors system, in a range of situations characterized by loading conditions and design parameters. For this purpose, the model accounts for bending and torsional deformations of the wing, pitch and yaw rotations of the propeller assemblies, gyroscopic effects, and thrust loads. Moreover, a vertical offsets between the wing elastic axis and the propeller axis is introduced to better represent the geometry of the pylons found in actual aircraft. Aerodynamic modeling is based on Theodorsen's unsteady thin-airfoil theory, converted to the time domain through Wagner's approximation.
This paper is organized as follows: section 2. summarizes the mathematical formulation underlying the structural and aerodynamic models, mass-unbalance excitation, thrust model, leading to the final coupled equations of motion. In section 3. the vibration responses obtained for numerical simulations performed for the different operating conditions are presented and discussed. Conclusions an final remarks are presented in section 4..

2. Mathematical Modeling

The system under investigation consists of a flexible wing equipped with two motor-propeller assemblies, as illustrated in Figs. 1a and 1b. The wing is modeled as a clamped-free structure, with the first propeller located at $0.31s$ from the wing root, where s denotes the semi-span length, and the second propeller mounted at the wing tip. The structural formulation is based on a finite element model of the wing, in which each beam element has six degrees of freedom associated with bending displacement, bending rotation, and torsional rotation at its two nodes. The propeller assemblies are attached to selected wing nodes and have pitch and yaw rotations. The wing aerodynamic loads are modeled based on Theodorsen's lift and pitching moment expressions and converted to the time domain through Wagner's approximation. Given the scope and length constraints of the present conference paper, propeller-induced aerodynamic effects, such as slipstream-wing interaction and blade-level unsteady loads, are not considered.The propellers are instead represented as rotating mechanical assemblies that contribute through prescribed thrust loads, gyroscopic effects, and mass-unbalance excitation.

2.1 Structural model

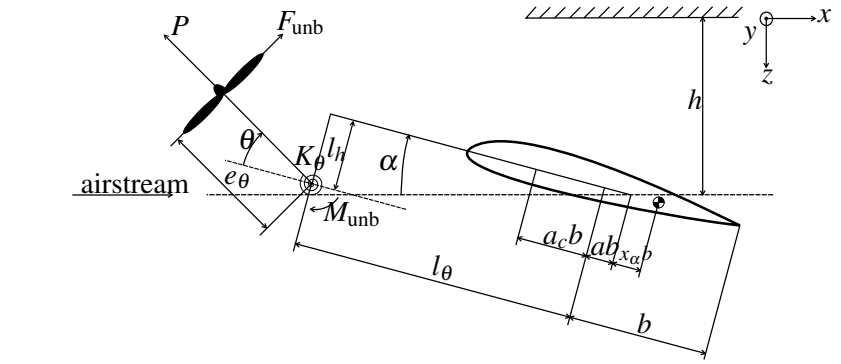
The structural model of the flexible wing is constructed based on the finite element approach, considering it as a variable-section cantilever Euler-Bernoulli beam subject simultaneously to bending and torsion deformations. From the geometry shown in Figs.1a and 1b, the vertical displacement of a generic point of the wing section can be written as

$$w(x,y,t) = h(y) + (x-ab)\alpha(y), \tag{1}$$

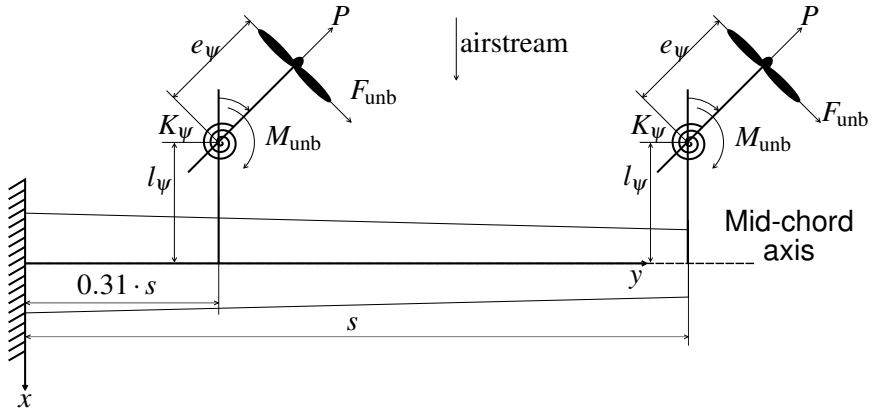
where $h(y)$ is the vertical displacement of the elastic axis, $\alpha(y)$ is the torsional rotation about the elastic axis, and ab denotes the distance between the elastic axis and the mid-chord reference point. The kinetic energy of the wing is given by

$$KE_w = \frac{1}{2}\int \dot{w}^2 dm = \frac{1}{2}\int m_w \dot{h}^2 dy + \frac{1}{2}\int m_w (x-ab)^2 \dot{\alpha}^2 dy + \int m_w (x-ab)\dot{\alpha}\dot{h} dy, \tag{2}$$

where m_w is the mass per length.



(a) Lateral view



(b) Top view

Figure 1 – Lateral and top views of a wing with two propellers driven by electric motors.

The corresponding strain energy is expressed as

$$PE_w = \frac{1}{2}\int GJ(\frac{\partial \alpha}{\partial y})^2 dy + \frac{1}{2}\int EI(\frac{\partial^2 h}{\partial y^2})^2 dy, \tag{3}$$

where GJ and EI is torsional and bending stiffness.
Within each finite element, the bending displacement h is approximated using cubic Hermite shape functions, while the torsional rotation α is interpolated using linear shape functions:

$$\begin{aligned} h &= h_i N_1 + \phi_i N_2 + h_{i+1} N_3 + \phi_{i+1} N_4 = \mathbf{N} \cdot \mathbf{h}^T, \\ \alpha &= \alpha_i T_1 + \alpha_{i+1} T_2 = \mathbf{T} \cdot \alpha^T. \end{aligned} \tag{4}$$

N_i and T_i are the shape function that ensure the continuity.
Substituting 4 in 2 and 3 we obtain the equation 5.

$$\begin{aligned} KE_w &= \frac{1}{2}\dot{\mathbf{h}}\mathbf{M_{e,b}}\dot{\mathbf{h}}^T + \frac{1}{2}\dot{\alpha}\mathbf{M_{e,t}}\dot{\alpha}^T + \mathbf{M_{e,tb}}\dot{\mathbf{h}}\dot{\alpha}, \\ PE_w &= \frac{1}{2}\mathbf{h}\mathbf{K_{e,b}}\mathbf{h}^T + \frac{1}{2}\alpha\mathbf{K_{e,t}}\alpha^T. \end{aligned} \tag{5}$$

Where $M_{e,b}$, $M_{e,t}$, $M_{e,tb}$, $K_{e,b}$ and $K_{e,t}$ is defined by the equations 6, 7, 8, 9, 10, where ρI_p is the torsional inertia and $x_a b$ is the distance between the center mass to the middle of the chord.

$$\mathbf{M}_{e,b} = \begin{bmatrix} \frac{13}{35}\ell_e m_w & \frac{11}{210}\ell_e^2 m_w & \frac{9}{70}\ell_e m_w & -\frac{13}{420}\ell_e^2 m_w \\ \frac{11}{210}\ell_e^2 m_w & \frac{1}{105}\ell_e^3 m_w & \frac{13}{420}\ell_e^2 m_w & -\frac{1}{140}\ell_e^3 m_w \\ \frac{9}{70}\ell_e m_w & \frac{13}{420}\ell_e^2 m_w & \frac{13}{35}\ell_e m_w & -\frac{11}{210}\ell_e^2 m_w \\ -\frac{13}{420}\ell_e^2 m_w & -\frac{1}{140}\ell_e^3 m_w & -\frac{11}{210}\ell_e^2 m_w & \frac{1}{105}\ell_e^3 m_w \end{bmatrix}. \tag{6}$$

$$\mathbf{M}_{e,t} = \begin{bmatrix} \frac{\rho I_p \ell_e}{3} & \frac{\rho I_p \ell_e}{6} \\ \frac{\rho I_p \ell_e}{6} & \frac{\rho I_p \ell_e}{3} \end{bmatrix}. \tag{7}$$

$$\mathbf{M}_{e,tb} = \begin{bmatrix} \frac{7}{20} m_w \ell_e x_a b & \frac{1}{20} m_w \ell_e^2 x_a b & \frac{3}{20} m_w \ell_e x_a b & -\frac{1}{30} m_w \ell_e^2 x_a b \\ \frac{3}{20} m_w \ell_e x_a b & \frac{1}{30} m_w \ell_e^2 x_a b & \frac{7}{20} m_w \ell_e x_a b & -\frac{1}{20} m_w \ell_e^2 x_a b \end{bmatrix}. \tag{8}$$

$$\mathbf{K}_{e,b} = EI \begin{bmatrix} \frac{12}{\ell_e^3} & \frac{6}{\ell_e^2} & -\frac{12}{\ell_e^3} & \frac{6}{\ell_e^2} \\ \frac{6}{\ell_e^2} & \frac{4}{\ell_e} & -\frac{6}{\ell_e^2} & \frac{2}{\ell_e} \\ -\frac{12}{\ell_e^3} & -\frac{6}{\ell_e^2} & \frac{12}{\ell_e^3} & -\frac{6}{\ell_e^2} \\ \frac{6}{\ell_e^2} & \frac{2}{\ell_e} & -\frac{6}{\ell_e^2} & \frac{4}{\ell_e} \end{bmatrix}. \tag{9}$$

$$\mathbf{K}_{e,t} = \begin{bmatrix} \frac{GJ}{\ell_e} & -\frac{GJ}{\ell_e} \\ -\frac{GJ}{\ell_e} & \frac{GJ}{\ell_e} \end{bmatrix}. \tag{10}$$

The final equation of the wing structural model can be defined by the equation 11, where inertia matrix of the wing $\mathbf{M}_{e,wing}$ is the combining of 6, 7 and 8 and the stiffness matrix of the wing $\mathbf{K}_{e,wing}$ is the combining of 9 and 10.

$$\mathbf{M}_{e,wing}\ddot{\mathbf{u}}_{e,wing} + \mathbf{C}_{e,wing}\dot{\mathbf{u}}_{e,wing} + \mathbf{K}_{e,wing}\mathbf{u}_{e,wing} = \mathbf{Q}_{e,wing}. \tag{11}$$

The structural damping of the wing is given by the Rayleigh Damping Theory, where we can address $\mathbf{C}_{e,wing}$ as $\mathbf{C}_{e,wing} = \mu\mathbf{M}_{e,wing} + \lambda\mathbf{K}_{e,wing}$.
The elemental vector of coordinates is $\mathbf{u}_{e,wing}$ that is expressed by:

$$\mathbf{u}_{e,wing} = [h_i, \phi_i, \alpha_i, h_{i+1}, \phi_{i+1}, \alpha_{i+1}]^T. \tag{12}$$

2.1.1 Propeller Structural Model

For the i-th propeller assembly, the vertical and lateral displacements of a generic point along the propeller axis are expressed as

$$\begin{aligned} z_{pi}(x,t) &= h_{pi} + l_{hi} + (x - a_{pi}b_{pi})\alpha_{pi} + (x - l_{\theta,i})\theta_i, \\ y_{pi}(x,t) &= -(x - l_{\psi,i})\psi_i. \end{aligned} \tag{13}$$

where h_{p_i} and α_{p_i} are, respectively, the bending displacement and torsional rotation of the wing node to which the propeller assembly is attached. The parameters $l_{h,i}$, $l_{\theta,i}$, and $l_{\psi,i}$ define the vertical offset and the pitch/yaw reference locations of the propeller assembly.
In addition, angular velocities of the propeller is defined as

$$\omega_{Xi} = \Omega_i + (\dot{\theta}_i + \dot{\alpha}_{pi}) \sin \psi_i \approx \Omega_i + (\dot{\theta}_i + \dot{\alpha}_{pi}) \psi_i, \tag{14}$$

where Ω_i is the rotation velocity of the i-th propeller.
The kinetic energy, $KE_{prop,i}$, can be divided into two parts: KE_{pi} that is the contribution of the non-rotating parts and $KE_{\Omega i}$ that is the contribution of the rotating parts. KE_{pi} is defined by equation 15

$$KE_{pi} = \frac{1}{2}\int m_{pi}(x)(\dot{z}_{pi}^2 + \dot{y}_{pi}^2)dx = \frac{1}{2}M_{pi}\dot{h}_{pi}^2 + \frac{1}{2}I_{\alpha,pi}\dot{\alpha}_{pi}^2 + \frac{1}{2}I_{\theta,pi}\dot{\theta}_i^{\,2} + S_{\alpha,pi}\dot{h}_{pi}\dot{\alpha}_{pi} + S_{\theta,pi}\dot{h}_{pi}\dot{\theta}_i + \frac{1}{2}I_{\psi,pi}\dot{\psi}_i^{\,2}. \tag{15}$$

where

$$\begin{aligned}
M_{pi} &= \int m_{pi}(x)\,dx, \\
S_{\alpha,pi} &= S_{\theta,pi} + (l_{\theta,i} - a_{pi}b_{pi})M_{pi}, \\
I_{\alpha,pi} &= \int m_{pi}(x)(x - a_{pi}b_{pi})^2 dx \\
&= I_{\theta,pi} + (l_{\theta i} - a_{pi}b_{pi})^2 M_{pi} + 2(l_{\theta i} - a_{pi}b_{pi})S_{\theta,pi},
\end{aligned}$$

with

$$\begin{aligned}
S_{\theta,pi} &= \int m_{pi}(x)(x - l_{\theta i})\,dx, \\
I_{\theta,pi} &= \int m_{pi}(x)(x - l_{\theta i})^2 dx, \\
I_{\psi,pi} &= \int m_{pi}(x)(x - l_{\psi i})^2 dx, \\
I_{\theta\alpha,pi} &= I_{\theta,pi} + (l_{\theta i} - a_{pi}b_{pi})S_{\theta,pi}.
\end{aligned} \tag{16}$$

For the $KE_{\Omega i}$ can be defined by the equation 17

$$KE_{\Omega i} = \frac{1}{2}I_{\Omega i}\omega_{Xi}^2 \approx \frac{1}{2}I_{\Omega i}\left[\Omega i^2 + 2\Omega i(\dot{\theta}_i + \dot{\alpha}_{pi})\psi_i\right] = \frac{1}{2}I_{\Omega i}\Omega i^2 + I_{\Omega i}\Omega_i\dot{\theta}_i\psi_i + I_{\Omega i}\Omega_i\dot{\alpha}_{pi}\psi_i.$$

The expression for the total kinetic energy for the $i'th$ propeller is

$$\begin{aligned}
KE_{prop,i} = {} & \frac{1}{2}M_{pi}\dot{h}_{pi}^2 + \frac{1}{2}I_{\alpha,pi}\dot{\alpha}_{pi}^2 + S_{\alpha,pi}\dot{h}_{pi}\dot{\alpha}_{pi} + \frac{1}{2}I_{\theta,pi}\dot{\theta}_{pi}^2 + S_{\theta,pi}\dot{h}_{pi}\dot{\theta}_{pi} \\
& + I_{\theta\alpha,pi}\dot{\alpha}_{pi}\dot{\theta}i + \frac{1}{2}I_{\psi,pi}\dot{\psi}_{pi}^2 + \frac{1}{2}I_{\Omega i}\Omega_i^2 + I_{\Omega i}\Omega_i\dot{\theta}_i\psi_i + I_{\Omega i}\Omega_i\dot{\alpha}_{pi}\psi_i.
\end{aligned}$$

Now, for the potential energy with the equation 17, where the the K_i terms can be defined by the uncoupled natural frequencies of the propeller.

$$PE_{prop,i} = \frac{1}{2}K_{\theta i}\theta_i^2 + \frac{1}{2}K_{\psi i}\psi_i^2. \tag{17}$$

Dissipation energy can be defined by the equation 18, with g_i being damping coefficients, ω the frequency vibration and ω_i the natural frequency of the pitch or yaw coordenate.

$$DE_{prop,i} = \frac{1}{2}\frac{K_{\theta i}g_{\theta i}}{\omega}\dot{\theta}_i^{\,2} + \frac{1}{2}\frac{K_{\psi_i}g_{\psi_i}}{\omega}\dot{\psi}_i^{\,2}. \tag{18}$$

Applying the Lagrange's equation in 17, 17, 18, we reach in the following equation of movement for the pitch θ_i and for yaw ψ_i:

$$\mathbf{M}_{ei,prop}\ddot{\mathbf{u}}_{ei,prop}+\mathbf{C}_{ei,prop}\dot{\mathbf{u}}_{ei,prop}+\mathbf{G}_{ei,prop}\dot{\mathbf{u}}_{wpi}+\mathbf{K}_{ei,prop}\mathbf{u}_{ei,prop}=\mathbf{Q}_{ei,prop}. \tag{19}$$

Where,

$$\mathbf{M}_{ei,prop}=\begin{bmatrix} I_{\theta,pi} & 0 \\ 0 & I_{\psi,pi}\end{bmatrix}. \tag{20}$$

$$\mathbf{K}_{ei,prop}=\begin{bmatrix} K_{\theta i} & 0 \\ 0 & K_{\psi i}\end{bmatrix}. \tag{21}$$

$$\mathbf{C}_{ei,prop}=\begin{bmatrix} \dfrac{K_{\theta i}g_{\theta i}}{\omega} & I_{\Omega i}\Omega_i \\ -I_{\Omega i}\Omega_i & \dfrac{K_{\psi i}g_{\psi i}}{\omega_i}\end{bmatrix}. \tag{22}$$

$$\mathbf{G}_{ei,prop}=\begin{bmatrix} 0 & 0 \\ 0 & -I_{\Omega i}\Omega_i\end{bmatrix}. \tag{23}$$

Also, $\mathbf{u}_{e,prop}=[\theta_i,\psi_i]^T$, $\mathbf{u}_{e,wp}=[h_{pi},\alpha_{pi}]^T$ and $\mathbf{Q}_{e,prop}$ is the generalized vector forces of pitch and yaw. In addition, we also reach to the equation for the contribution of the propeller for the h_{pi} and α_{pi} given by:

$$\mathbf{M}_{ei,wp}\ddot{\mathbf{u}}_{ei,prop}+\mathbf{A}_{ei,wp}\ddot{\mathbf{u}}_{ei,wp}+\mathbf{G}_{ei,wp}\dot{\mathbf{u}}_{ei,prop}=\mathbf{Q}_{ei,wp}, \tag{24}$$

where,

$$\mathbf{M}_{ei,wp}=\begin{bmatrix} S_{\theta,pi} & 0 \\ I_{\theta\alpha,pi} & 0\end{bmatrix}. \tag{25}$$

$$\mathbf{A}_{ei,wp}=\begin{bmatrix} M_{pi} & S_{\alpha,pi} \\ S_{\alpha,pi} & I_{\alpha,pi}\end{bmatrix}. \tag{26}$$

$$\mathbf{G}_{ei,wp}=\begin{bmatrix} 0 & 0 \\ 0 & I_{\Omega i}\Omega_i\end{bmatrix}. \tag{27}$$

2.2 Aerodynamics

The aerodynamic model adopted in this work is based on Theodorsen's unsteady thin-airfoil theory. The frequency-domain lift and pitching moment expressions are converted to the time domain using Wagner's approximation, allowing the aerodynamic forces to be coupled with the structural equations of motion in transient simulations. By the Theodorsen's theory the section lift and the section pitching moment about the elastic is given by

$$L=\pi\rho b^2\left(\ddot{h}+V\dot{\alpha}-ba\ddot{\alpha}\right)+2\pi\rho VbC(k)w, \tag{28}$$

$$\begin{aligned} M=&\pi\rho b^2\left[ab\ddot{h}-Vb\left(\frac{1}{2}-a\right)\dot{\alpha}-b^2\left(\frac{1}{8}+a^2\right)\ddot{\alpha}\right] \\ &+2\pi\rho Vb^2\left(a+\frac{1}{2}\right)C(k)w \end{aligned}.$$

where V is the airstream velocity, ρ is the air density, and w is the total aerodynamic downwash at the three-quarter chord position that is addressed as

$$w=\dot{h}+V\alpha+b\left(\frac{1}{2}-a\right)\dot{\alpha}. \tag{29}$$

Bringing to the time domain, by the Wagner's method, is determined the relations 30, 31, 31

$$\Phi(t) = 1 - \Psi_1 e^{-\varepsilon_1 \frac{V}{b} t} - \Psi_2 e^{-\varepsilon_2 \frac{V}{b} t}. \tag{30}$$

$$\begin{aligned}
C(k)w &= \Phi(0)w(t) - \int_0^t \frac{d\Phi(t-t_0)}{dt_0} w(t_0)\, dt_0 \\
&= \Phi(0)w(t) - \left[h(0) + b\left(\frac{1}{2} - a\right)\alpha(0)\right]\dot{\Phi}(t) \\
&\quad + \left[h(t) + b\left(\frac{1}{2} - a\right)\alpha(t)\right]\dot{\Phi}(0) \\
&\quad - \Psi_1 \left(\frac{\varepsilon_1 V}{b}\right)^2 w_1(t) - \Psi_2 \left(\frac{\varepsilon_2 V}{b}\right)^2 w_2(t) \\
&\quad + \Psi_1 \frac{\varepsilon_1 V^2}{b}\left[1 - \varepsilon_1\left(\frac{1}{2} - a\right)\right] w_3(t) \\
&\quad + \Psi_2 \frac{\varepsilon_2 V^2}{b}\left[1 - \varepsilon_2\left(\frac{1}{2} - a\right)\right] w_4(t) \\
\dot{w}_1(t) &= h(t) - \frac{\varepsilon_1 V}{b} w_1(t) \\
\dot{w}_2(t) &= h(t) - \frac{\varepsilon_2 V}{b} w_2(t) \\
\dot{w}_3(t) &= \alpha(t) - \frac{\varepsilon_1 V}{b} w_3(t) \\
\dot{w}_4(t) &= \alpha(t) - \frac{\varepsilon_2 V}{b} w_4(t)
\end{aligned} \tag{31}$$

Combining the equations above, we can determine the aerodynamics matrices of inertia $\mathbf{M}_{s,aw}$, damping $\mathbf{C}_{s,aw}$ and stiffness $\mathbf{K}_{s,aw}$ besides the lag-state equations W_i's for a wing section

$$\mathbf{M}_{s,aw} = \begin{bmatrix} -\pi\rho b^2 & \pi\rho b^3 a \\ \pi\rho b^3 a & -\pi\rho b^4\left(\frac{1}{8} + a^2\right) \end{bmatrix}. \tag{32}$$

$$\mathbf{C}_{s,aw} = \begin{bmatrix} -2\pi\rho b V \Phi(0) & -\pi\rho b^2 V - 2\pi\rho b^2 V\left(\frac{1}{2} - a\right)\Phi(0) \\ 2\pi\rho b V \Phi(0) b\left(a + \frac{1}{2}\right) & -\pi\rho b^3 V\left(\frac{1}{2} - a\right) + 2\pi\rho b^2 V\left(\frac{1}{2} - a\right)\Phi(0) b\left(a + \frac{1}{2}\right) \end{bmatrix}. \tag{33}$$

$$\mathbf{K}_{s,aw} = \begin{bmatrix} -2\pi\rho b V \dot{\Phi}(0) & -2\pi\rho b V^2 \Phi(0) - 2\pi\rho b^2 V\left(\frac{1}{2} - a\right)\dot{\Phi}(0) \\ 2\pi\rho b V \dot{\Phi}(0) b\left(a + \frac{1}{2}\right) & 2\pi\rho b V^2 \Phi(0) b\left(a + \frac{1}{2}\right) + 2\pi\rho b^2 V\left(\frac{1}{2} - a\right)\dot{\Phi}(0) b\left(a + \frac{1}{2}\right) \end{bmatrix}. \tag{34}$$

$$\mathbf{W}_0 = 2\pi\rho b V \mathbf{W}_0' \tag{35}$$

$$\mathbf{W}_0' = \begin{bmatrix} \Psi_1\left(\varepsilon_1 \frac{V}{b}\right)^2 & \Psi_2\left(\varepsilon_2 \frac{V}{b}\right)^2 & -\Psi_1 \varepsilon_1 \frac{V^2}{b}\left[1 - \varepsilon_1\left(\frac{1}{2} - a\right)\right] & -\Psi_2 \varepsilon_2 \frac{V^2}{b}\left[1 - \varepsilon_2\left(\frac{1}{2} - a\right)\right] \\ -\Psi_1\left(\varepsilon_1 \frac{V}{b}\right)^2 b\left(a + \frac{1}{2}\right) & -\Psi_2\left(\varepsilon_2 \frac{V}{b}\right)^2 b\left(a + \frac{1}{2}\right) & \Psi_1 \varepsilon_1 \frac{V^2}{b}\left[1 - \varepsilon_1\left(\frac{1}{2} - a\right)\right] b\left(a + \frac{1}{2}\right) & \Psi_2 \varepsilon_2 \frac{V^2}{b}\left[1 - \varepsilon_2\left(\frac{1}{2} - a\right)\right] b\left(a + \frac{1}{2}\right) \end{bmatrix}. \tag{36}$$

$$\mathbf{W}_1 = \begin{bmatrix} 1 & 0 \\ 1 & 0 \\ 0 & 1 \\ 0 & 1 \end{bmatrix}. \tag{37}$$

$$\mathbf{W}_2 = \begin{bmatrix} -\frac{\varepsilon_1 V}{b} & 0 & 0 & 0 \\ 0 & -\frac{\varepsilon_2 V}{b} & 0 & 0 \\ 0 & 0 & -\frac{\varepsilon_1 V}{b} & 0 \\ 0 & 0 & 0 & -\frac{\varepsilon_2 V}{b} \end{bmatrix}. \tag{38}$$

The final expression that's represents the movement equation influenced by the aerodynamical of the wing can be expressed as:

$$\begin{aligned} &(\mathbf{M}_{wing} - \mathbf{M}_{aw})\ddot{\mathbf{u}}_{wing} + (\mathbf{C}_{wing} - \mathbf{C}_{aw})\dot{\mathbf{u}}_{wing} + (\mathbf{K}_{wing} - \mathbf{K}_{aw})\mathbf{u}_{wing} = \mathbf{W}_{\mathbf{w},\mathbf{0}}\mathbf{w}_{\mathbf{w}} \\ &\dot{\mathbf{w}}_w = \mathbf{W}_{w,1}\mathbf{u}_{wing} + \mathbf{W}_{w,2}\mathbf{w}_{\mathbf{w}}, \end{aligned} \tag{39}$$

where $\mathbf{M}_{wing}$, $\mathbf{C}_{wing}$, $\mathbf{K}_{wing}$ are structual matrices of the wing, $\mathbf{M}_{aw}$, $\mathbf{C}_{aw}$, $\mathbf{K}_{aw}$ $\mathbf{W}_{w,i}$ are the aerodynamics matrices developed at this subsection assembled in the wing system as proposed by Xu [3].

2.3 Unbalancing

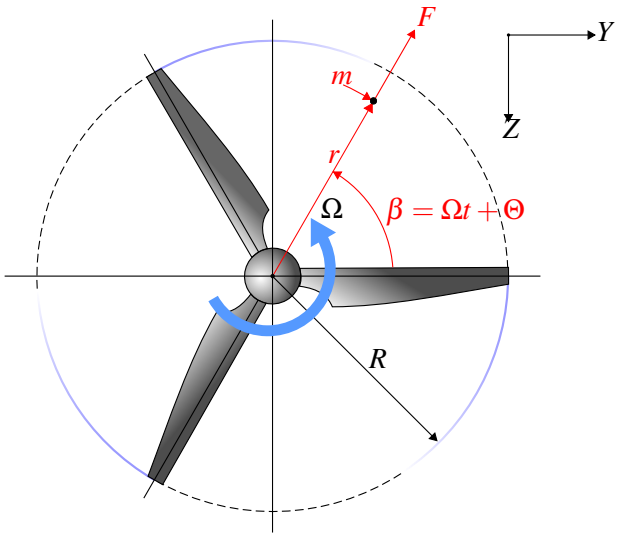


Figure 2 – Equivalent mass-unbalance scheme

According to [13], the harmonic force generated by an eccentric mass attached to a rotating system can be expressed as

$$\begin{aligned} F_{unb} &= m_{unb} \cdot r \cdot \Omega^2, \\ F_{unb,z} &= F_{unb} \cdot \sin(\Omega t + \Theta), \\ F_{unb,y} &= F_{unb} \cdot \cos(\Omega t + \Theta). \end{aligned} \tag{40}$$

where m_{unb} is the unbalanced mass, r is the eccentricity radius, Ω is the angular velocity, and Θ is the initial phase angle.
The corresponding moments generated by the unbalance force are given by

$$\begin{aligned} M_{unb,\theta} &= F_{unb,z} \cdot e_\theta, \\ M_{unb,\psi} &= F_{unb,y} \cdot e_\psi. \end{aligned} \tag{41}$$

The force $F_{unb,zi}$ acts in the degree of freedom z_{pi}, and the moments $M_{unb,\theta i}$ and $M_{unb,\psi i}$ acts in the degree of freedom θ_i and ψ_i respectively.

2.4 Thrust

The thrust model adopted in this work follows Gudmundsson [15]. The propeller thrust is estimated from the available motor power as

$$P_i = \frac{\eta_{pi} \cdot Pot_i}{V}, \tag{42}$$

with,

$$\eta_{pi} = 0.096574 + 1.703049 J_i - 0.952281 J_i^2, \tag{43}$$

and,

$$J_i = \frac{60 \times V}{\Omega_{rpm,i} \times D_i}, \tag{44}$$

where Pot is the motor power, η_p is the propeller efficiency, and J is the advance ratio.
By the configuration as Fig. 1a, we can determinate that thrust acts in the nodes z_{pi} and α_{pi} as,

$$\begin{aligned} F_{thrust,zi} &= P_i \sin(\theta + \alpha) \\ M_{thrust,\alpha i} &= P_i \sin(\theta)(e_\theta + l_{\theta i}) - P_i \cos(\theta)(l_h - e_\theta \sin(\theta)) \end{aligned} \tag{45}$$

2.5 Coupled equations of motion

The elemental matrices and force vectors derived in the previous subsections are assembled into a global coordinate system containing the wing structural DOFs, the propeller pitch and yaw DOFs, and the aerodynamic lag states. The resulting coupled aeroelastic equation of motion is written as

$$\begin{aligned} &(\mathbf{M}_{g,wing} - \mathbf{M}_{g,aw} + \mathbf{A}_{g,wp1} + \mathbf{M}_{g,p1} + \mathbf{M}_{g,wp1} + \mathbf{A}_{g,wp2} + \mathbf{M}_{g,p2} + \mathbf{M}_{g,wp2})\ddot{\mathbf{u}}_{global} + \\ &(\mathbf{C}_{g,wing} - \mathbf{C}_{g,aw} + \mathbf{G}_{g,p1} + \mathbf{C}_{g,p1} + \mathbf{G}_{g,wp1} + \mathbf{G}_{g,p2} + \mathbf{C}_{g,p2} + \mathbf{G}_{g,wp2})\dot{\mathbf{u}}_{global} + \\ &(\mathbf{K}_{g,wing} - \mathbf{K}_{g,aw} + \mathbf{K}_{g,p1} + \mathbf{K}_{g,p2})\mathbf{u}_{global} = \mathbf{Q}_{global} + \mathbf{W}_{\mathbf{g},\mathbf{0}}\mathbf{w}_{\mathbf{g}}, \\ &\dot{\mathbf{w}}_{\mathbf{g}} = \mathbf{W}_{g,1}\mathbf{u}_{global} + \mathbf{W}_{g,2}\mathbf{w}_g. \end{aligned} \tag{46}$$

with,

$$\mathbf{u}_{global} = \begin{bmatrix} \mathbf{u}_{wing} \\ \mathbf{u}_{prop1} \\ \mathbf{u}_{prop2} \end{bmatrix}. \tag{47}$$

where $\mathbf{u}_{wing}$ contains the bending and torsional DOFs of the wing, while $\mathbf{u}_{prop_1}$ and $\mathbf{u}_{prop_2}$ contain the pitch and yaw DOFs of each propeller assembly. The attachment DOFs associated with each propeller are already included in $\mathbf{u}_{wing}$.

3. Analysis and Discussion

The numerical results are organized to investigate the influence of three parameters on the vibration response of the coupled wing-propeller system: the mismatch between propeller rotational speeds, the phase difference between the unbalance forces, and the vertical offset between the wing elastic axis and the propeller axis. For each condition, the purely structural response is compared with the aeroelastic response in order to identify the contribution of the aerodynamic coupling to the transient behavior, steady-state amplitude, and mean displacement of the wing.

3.1 Simulation Conditions and Response Evaluation

The baseline configuration, based on [14], [3], [5], is defined from the data presented in Tables 1a,1b and 2, which summarize the wing properties, propeller parameters, and flight operating condition. The response quantity analyzed in the following subsections is the vertical displacement at the wing tip.

Unless otherwise stated, the amplitudes discussed in this section correspond to the steady-state oscillatory component of the response after the initial transient has decayed.

Table 1 – Baseline wing and propeller data

Parameter	Value	Unit
Half wing span	5.7	m
Root chord	1.25	m
Tip chord	0.8	m
Thickness-to-chord	15%	-
Mass per unit length	25	Kg/m
Radius of gyration (about CG)	25%	-
Spanwise elastic axis (from LE)	50%	-
Centre of gravity (from LE)	50%	-
Bending rigidity (EI)	$7 \cdot 10^5$	N.m^2
Torsional rigidity (GJ)	$2 \cdot 10^5$	N.m^2
Aerodynamic centre ac (from LE)	25%	-
Lift curve slope C_{l_α}	2π	-

(a) Baseline wing data

Parameter	Value	Unit
Number of blades	3	-
Rotor diameter	1.524	m
Hub diameter	0.25	m
Motor diameter	0.3556	m
Rotor mass	8	kg
Motor-nacelle mass	35	kg
Position of rotor CG	-1.16	m
Position of motor CG	-0.86	m
$l_\theta = l_\psi$	0	m
$e_\theta = e_\psi$	-1.16	m
$f_\theta = f_\psi$	7	Hz
$g_\theta = g_\psi$	0.005	-
Maximum power of motor	60	kW
Percent power used	75%	-

(b) Baseline propeller data

Table 2 – Flight operation condition

Parameter	Value	Unit
Cruise speed	77	m/s
Altitude	2438.4	m
Density of air	0.96	kg/m^3

In order to compare the cases without prescribing a specific eccentric mass, the unbalance coefficient $m_{unb} \cdot r$ was set to unity. Therefore, the unbalance force scales with the square of the rotational speed,$F_{unb} = (m_{unb} \cdot r) \cdot \Omega^2$ N .

3.2 Effect of Propeller Speed Mismatch

When the two propellers operate at slightly different rotational speeds, the corresponding unbalance forces act at different excitation frequencies. As a consequence, the wing response presents a beating pattern, characterized by a high-frequency oscillation modulated by a low-frequency envelope. The period of this envelope increases as the speed mismatch $\Delta\Omega$ decreases, which explains the more clearly defined amplitude modulation observed for the lower mismatch cases.

For the Structural case with the propeller 1 mismatch speed show in Fig. 3 is observed a increase of amplitude, A in stationary response with the decrease of $\Delta\Omega$, starting with $A \approx 0.018$ m for $\Delta\Omega = 1$ Hz, reaching $A \approx 0.022$ m for $\Delta\Omega = 0.2$ Hz.

Another analysis to be made is the changing of the propeller that has the rotating speed mismatch. The Fig. 4 represents the effect of the $\Delta\Omega$ changing for the propeller 2. The beating phenomenon keeps the same tends of the case before, but the amplitude show a different behavior. The amplitude, A increases with the increasing of $\Delta\Omega$, for $\Delta\Omega = 1$ Hz, $A \approx 0.032$m and for $\Delta\Omega = 0.2$ Hz, $A \approx 0.024$ m.

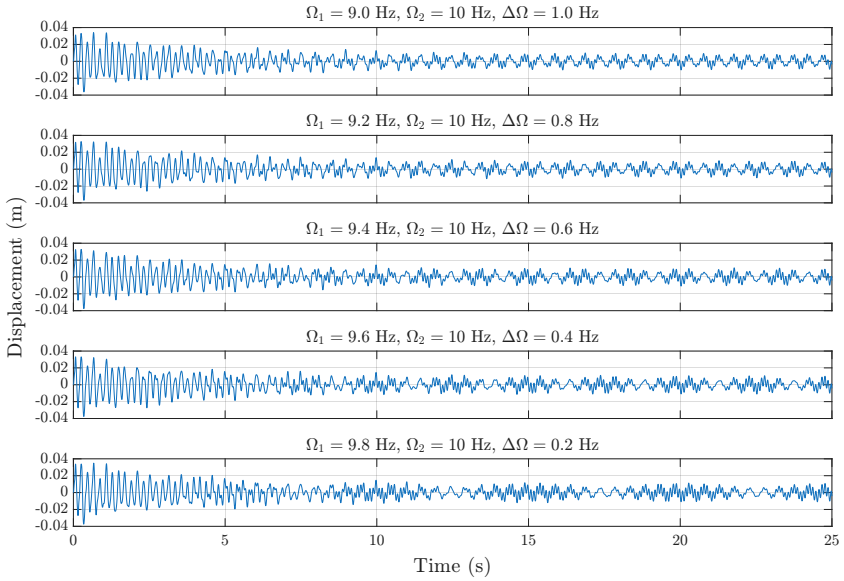


Figure 3 – Structural response with propeller 1 mismatch

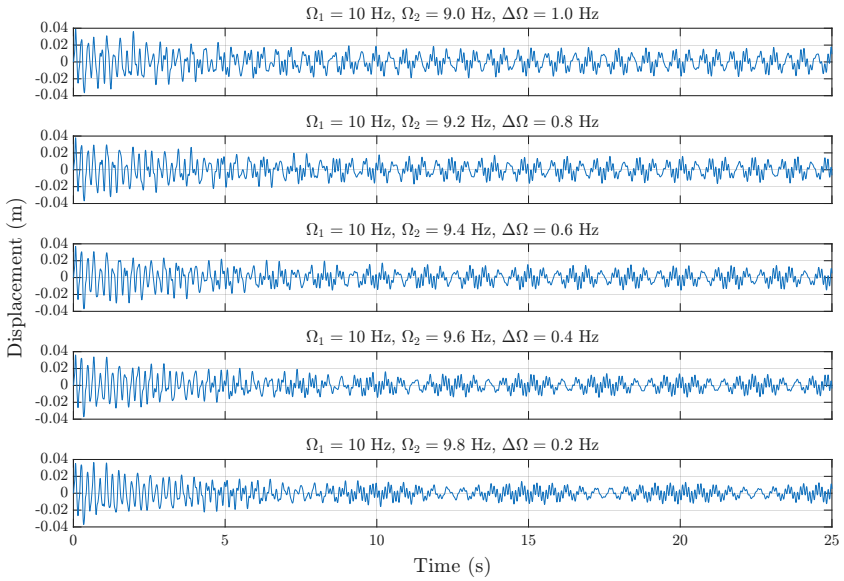


Figure 4 – Structural response with propeller 2 mismatch

The comparison between Figs.3 and 4 shows that the effect of the speed mismatch is not governed only by the magnitude of $\Delta\Omega$, but also by the spanwise location of the propeller operating under the mismatch condition. When the mismatch is applies to the propeller 1, the steady-state amplitude varies, increasing by approximately 18% as $\Delta\Omega$ decreases. In contrast, when the same is applies to the propeller 2, the amplitude decreases about 25%. This difference indicates that the same rotational-speed mismatch may produce different vibration levels depending on the propeller location, due to the different dynamic participation associated with each excitation point. Therefore, in DEP configurations, off-nominal propeller operation should be evaluated not only in terms of the mismatch magnitude, but also in terms of where the mismatch occurs along the wing span.

The aeroelastic responses show the same qualitative beating behavior, but with significantly damping vibration than the structural cases, and higher amplitudes in the stationary response. This behavior indicates that the unsteady aerodynamic model in this condition modified the damping and the stiffness of the system.

The same behavior of the amplitudes of the earlier cases are observed for this both cases. In Fig. 5 the amplitude varies from $A \approx 0.032$ m for the case of $\Delta\Omega = 1$ Hz $A \approx 0.036$ m for $\Delta\Omega = 0.2$ Hz, one increase of almost 11%

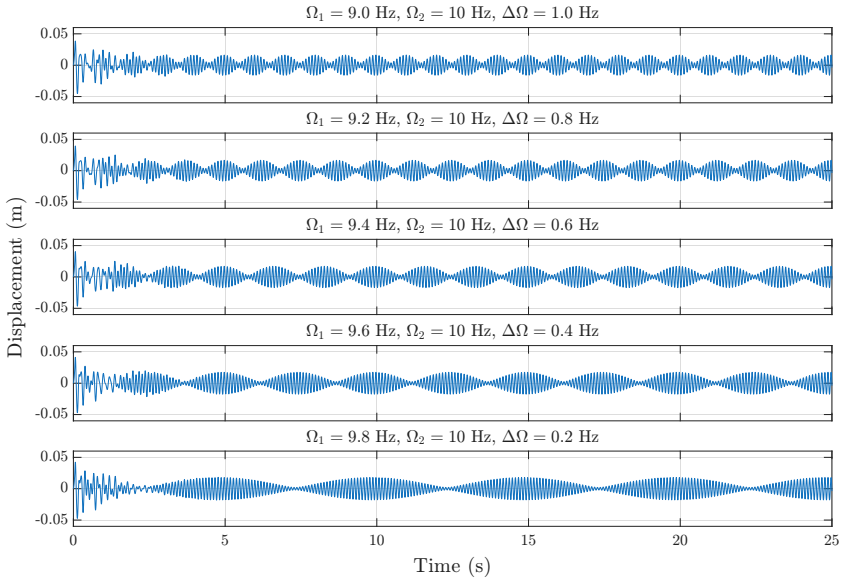


Figure 5 – Aeroelastic response with propeller 1 mismatch

For the Fig.6 the amplitude behavior is the same as Fig.4, in $\Delta\Omega = 1$ Hz has the amplitude of $A \approx 0.067$ m and for $\Delta\Omega = 0.2$ Hz the amplitude of the stationary phase is $A \approx 0.057$ m, one decrease of 15%.

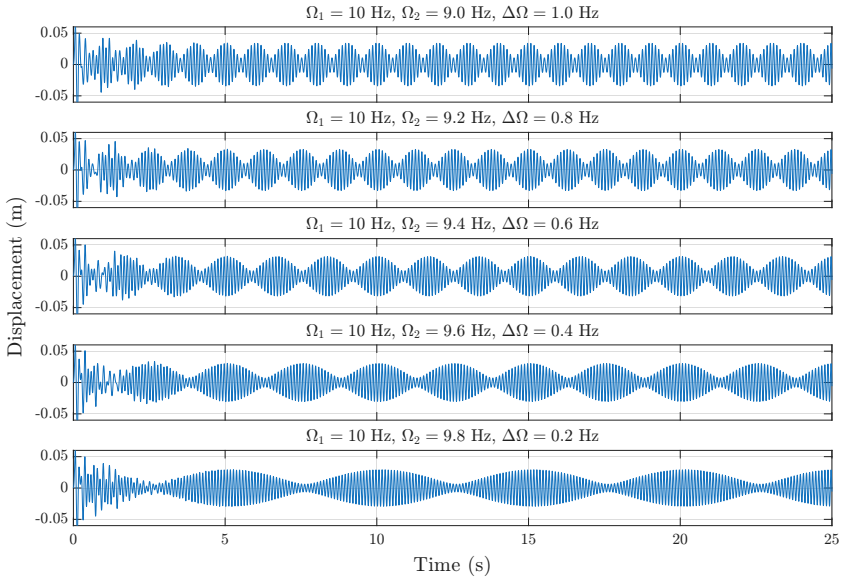


Figure 6 – Aeroelastic response with propeller 2 mismatch

The four conditions showed in this subsection indicates how the speed mismatch can affect the propeller-wing structure. The vary of the $\Delta\Omega$ affect the beating phenomenon all the cases with the same tends, varying the beating frequency, that is the expect in this situation. Add to this the changing in the intensity and behavior of the amplitude, showing the impact of which propeller the fail occurs, important information in a context when there is more than 1 propeller like a DEP configuration.
Overall, the four sets of results analyzed in this subsection show that the speed mismatch affects both the modulation frequency of the beating response and the corresponding steady-state amplitude. In all cases, decreasing $\Delta\Omega$ increases the beating period, as expected from the superposition of two close excitation frequencies. However, the amplitude trend depends on which propeller is subjected to the mismatch, showing that the spanwise position of the excitation plays an important role in the vibration response. This result is particularly relevant for DEP configurations, in which multiple propulsors may operate under slightly different rotational speeds and excite the flexible wing with different modal participation factors.

3.3 Effect of Phase Difference Between Unbalance Forces

Observing the Fig.7,8,9,10 is notable the influence of different phases on the amplitude of the displacement. The phase difference modifies the constructive and destructive superposition of the unbalance forces. As $\Delta\Theta$ increases, the resultant generalized force acting on the measured wing response is reduced, leading to lower steady-state amplitudes and a less pronounced beating envelope. The minimum response occurs close to the anti-phase condition, although complete cancellation is not expected because the propellers are attached at different spanwise positions and the coupled structural modes are not perfectly symmetric.

For the Fig. 7 and Fig.8 the amplitude starts with $A \approx 0.024$ m for the same-phase condition and $A \approx 0.008$ m for the anti-phase condition.

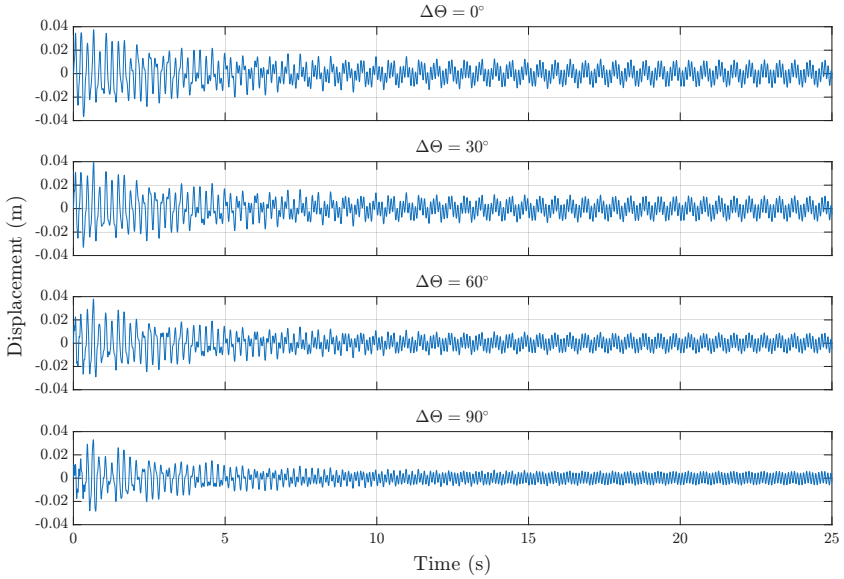


Figure 7 – Structural response for $0° < \Delta\Theta < 90°$

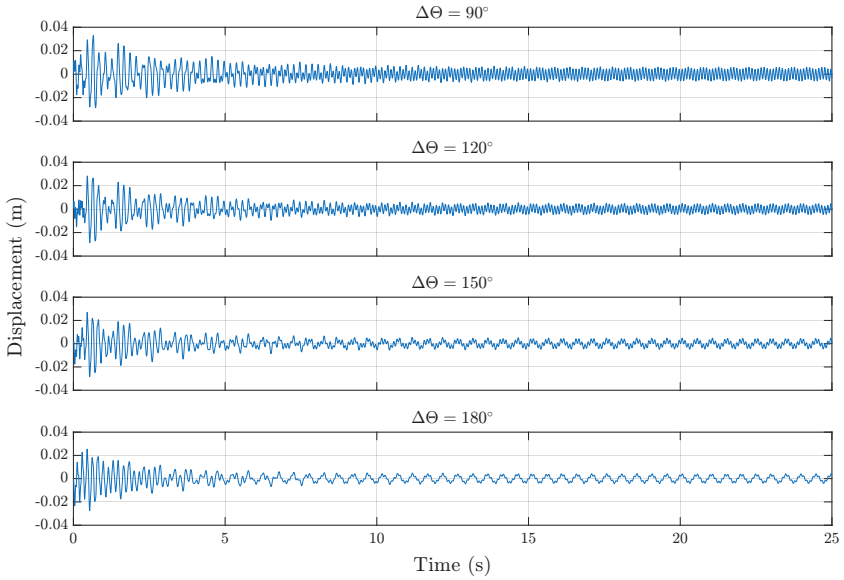


Figure 8 – Structural response for $90° < \Delta\Theta < 180°$

These results indicate that the phase difference mainly controls the constructive and destructive superposition of the unbalance forces. Unlike the speed-mismatch cases, in which the beating envelope is governed by the difference between excitation frequencies, the phase-difference cases modify the resultant forcing level applied to the structure. As the phase difference approaches the anti-phase condition, the generalized forces transmitted to the wing partially cancel each other, reducing the

steady-state displacement amplitude.
The decrease of amplitude is also observed in the aeroelastic case, with a decrease more aggressive than the structural case, influenced by the stiffness and damping aerodynamic. For the same-phase condition presented in Fig.9, amplitude is $A \approx 0.036$ m and for the anti-phase condition represented by Fig.10 the amplitude is given by $A \approx 0.006$ m

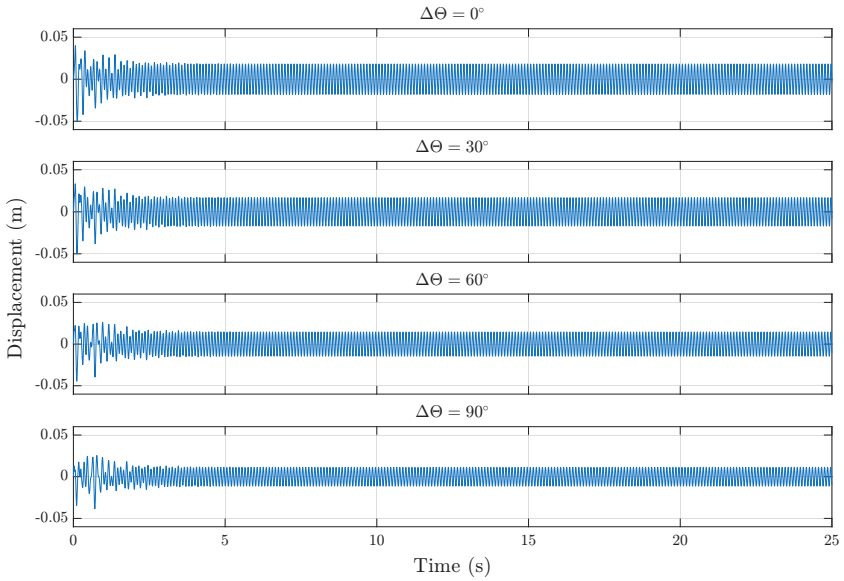


Figure 9 – Aeroelastic response for $0° < \Delta\Theta < 90°$

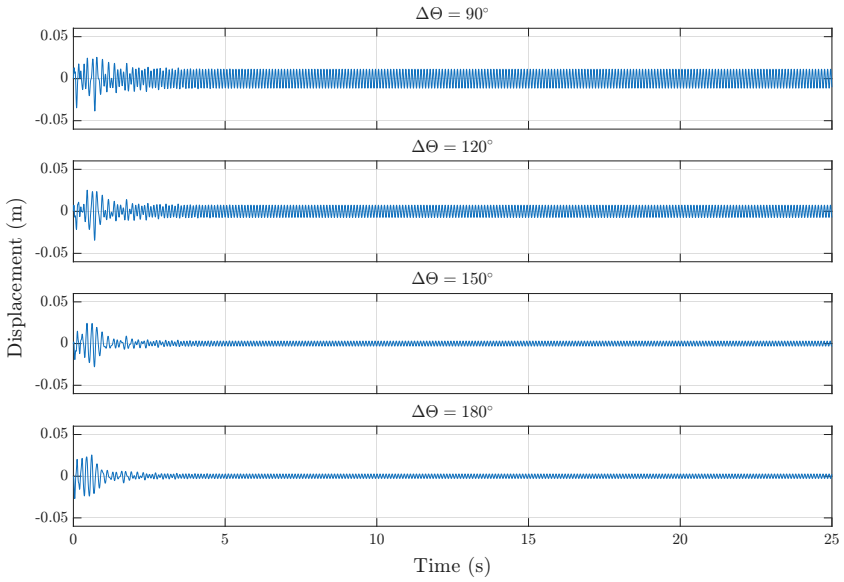


Figure 10 – Aeroelastic response for $90° < \Delta\Theta < 180°$

The aeroelastic results follow the same phase-dependent trend observed in the structural model, with the amplitude decreasing as $\Delta\Theta$ approaches the anti-phase condition. However, the comparison between structural and aeroelastic amplitudes is not uniform for all phase differences. For the same-phase condition, the aeroelastic response presents a higher stationary amplitude than the purely structural response, whereas near the anti-phase condition the aeroelastic amplitude becomes lower. This behavior indicates that aerodynamic coupling changes the effective dynamic participation of the system and that the phase difference acts directly on the resultant harmonic forcing transmitted to the wing.

3.4 Influence of the Vertical Offset Between Wing and Propeller Axis

In previous analyses, the propeller axis was assumed to be aligned with the wing elastic axis. However, in a real DEP configuration may be exist a vertical offset between this axis. This offset modifies the moment caused by the thrust, that changes the response of the structure. Also the inclusion of the vertical offset add a mean displacement. The thrust-induced moment shifts the equilibrium position of the wing,producing a nonzero mean displacement around which the vibration takes place. Therefore, the offset changes the response in two distinct ways: it increases the oscillatory vibration level and modifies the static or quasi-static equilibrium position of the coupled aeroelastic system.
To evaluate this effect, the same speed-mismatch and phase-difference cases discussed in the previous subsections are repeated considering a vertical offset of $l_h = 0.05$ m.
For the structures cases, the effects of offset inclusion was more notice in amplitude displacement. In the Fig.11 the amplitudes varies between $A \approx 0.036$ m and $A \approx 0.040$ m, that compared with the observed in the Fig. 3, represents a increase in the amplitude. Also the equilibrium shift, z_0 is approximately constant, with both cases $z_0 \approx -0.016$ m.

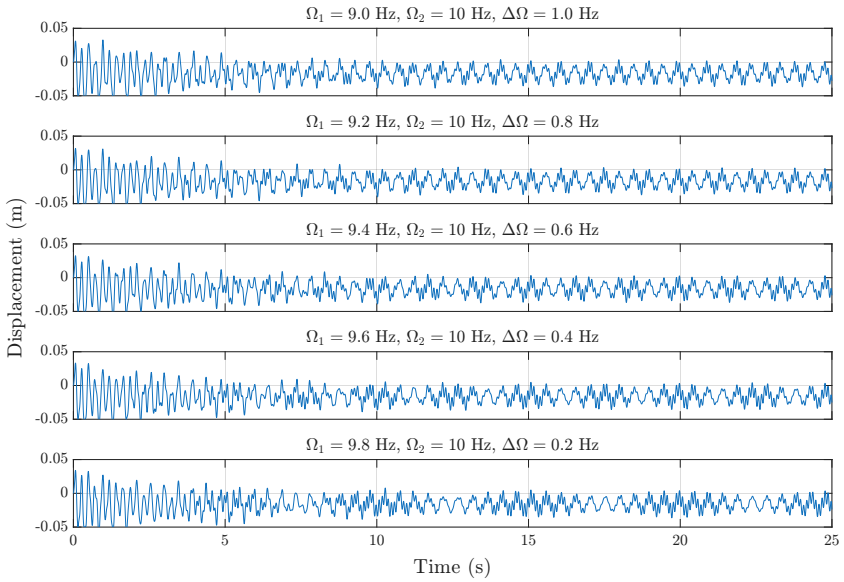


Figure 11 – Structural response with propeller 1 mismatch

The same behavior is seen for different phases case, as is show in Fig.12 and 13 that have a vary of amplitudes that begin with $A \approx 0.041$ m for 0° phase condition, and for 180° the amplitude observed is $A \approx 0.015$m. The z_0 was the approximately the same observed in the condition before.
The structural results show that the offset increases the oscillatory displacement amplitude when compared with the aligned-axis configuration and changed the equilibrium position. This behavior is associated with the additional moment arm introduced by l_h, which intensifies bending-torsional motion of the wing. The phase-difference effect is still present, since the anti-phase condition reduces the resultant harmonic excitation, but the overall vibration level remains higher than in the corresponding no-offset cases.
For the aeroelastic simulations, the offset affects both the oscillatory amplitude and the mean displacement. In contrast with the structural model, the aeroelastic equilibrium shift occurs in the opposite direction, suggesting that the interaction between the aerodynamic loads and the thrust-induced moment modifies the static or quasi-static balance of the coupled system. Therefore, the offset should not be interpreted only as an additional structural moment arm, but also as a parameter that changes the aeroelastic equilibrium position.
For the mismatch cases, show by Fig.14 have a increase of the amplitude as seen in the structural case. For $\Delta\Omega = 1$ Hz the amplitude is $A \approx 0.040$ m and for the $\Delta\Omega = 0.2$ Hz case the amplitude found is $A \approx 0.075$ m, which corresponds to a increase in the amplitude for the cases seen in subsection 3.2 . Also is notice a increasing of the equilibrium shift, z_0 between $\Delta\Omega = 1$ case and $\Delta\Omega = 0.2$, for the first case $z_0 \approx 0.040$ m and for the second case $z_0 \approx 0.054$ m, this difference shows in contrast with

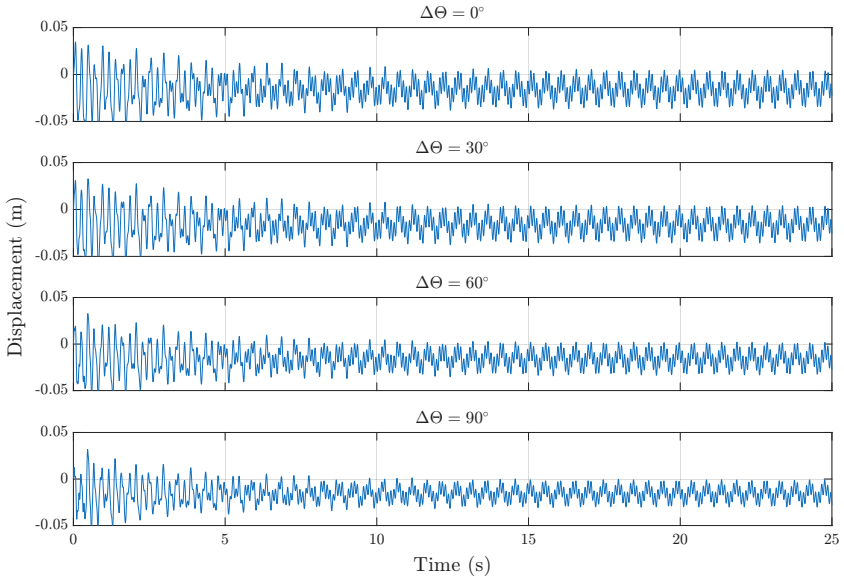


Figure 12 – Structural response for $0° \leq \Delta\Theta \leq 90°$ and $l_h = 0.05m$

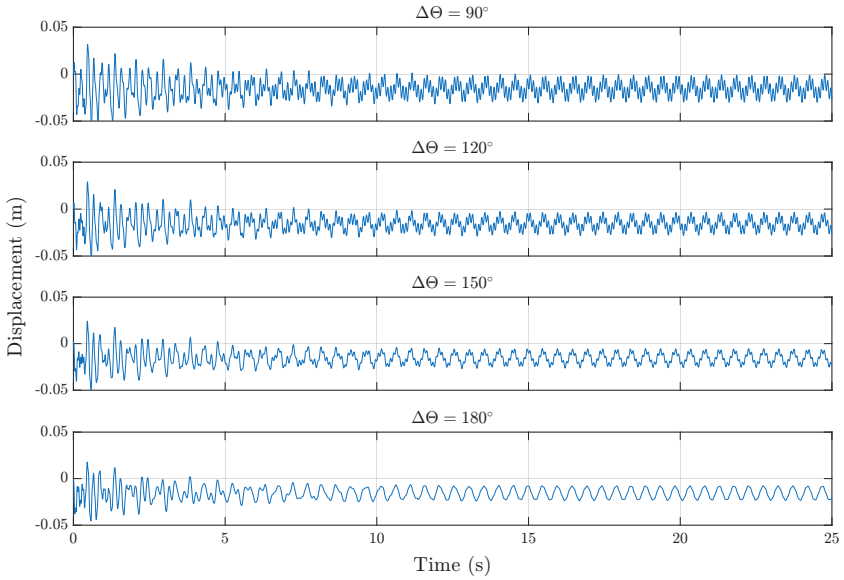


Figure 13 – Structural response for $90° \leq \Delta\Theta \leq 180°$ and $l_h = 0.05m$

the structural cases, for aeroelastisc analyses with the offset, the mismatch speeds also affects the equilibrium position.

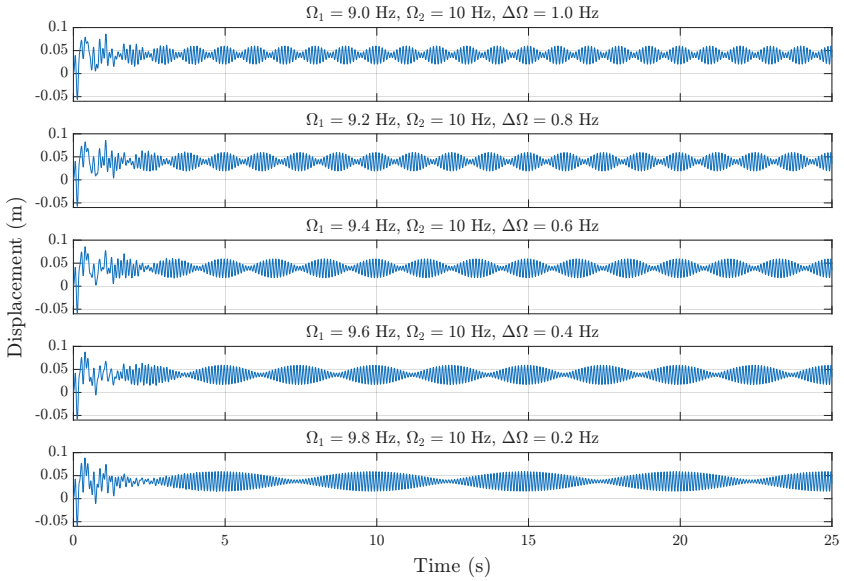


Figure 14 – Aeroelastic response with propeller 1 mismatch and $l_h = 0.05m$

For the different phase scenario, represented by Fig.15 and 16, the difference between amplitudes is also observed, but the influence in mean displacement is not observed. In same-phase condition the amplitude is $A \approx 0.043$ m and in anti-phase the amplitude is $A \approx 0.007$, but in both cases the offset is $z_0 \approx 0.0365$m.

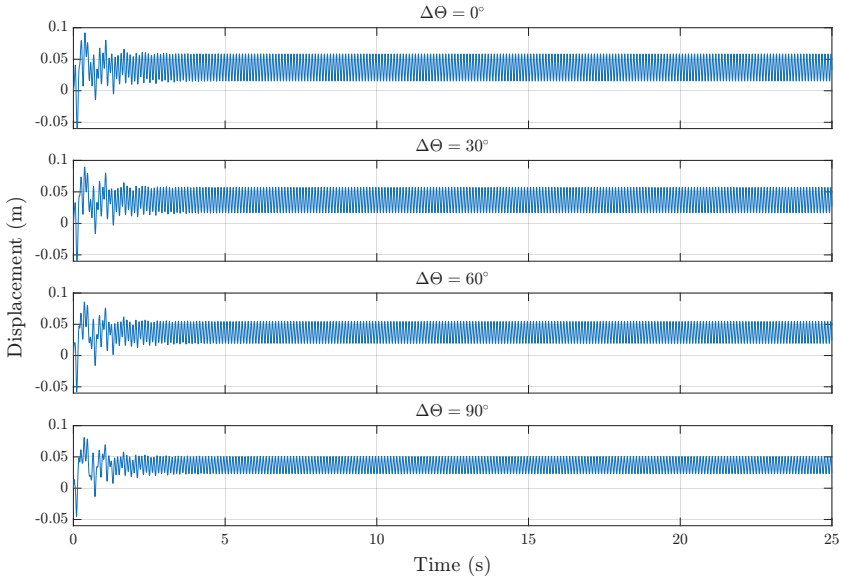


Figure 15 – Aeroelastic response for $0° < \Delta\Theta < 90°$ and $l_h = 0.05m$

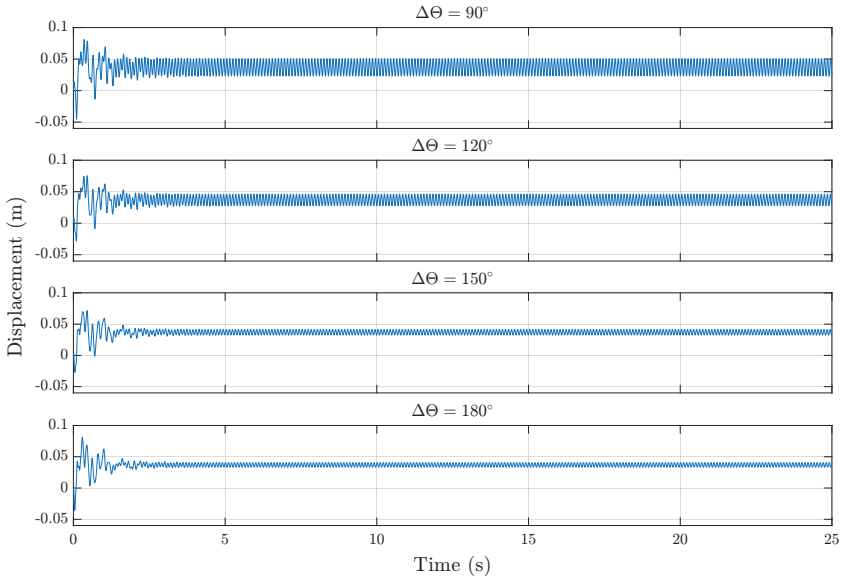


Figure 16 – Aeroelastic response for $90° < \Delta\Theta < 180°$ and $l_h = 0.05m$

In the phase-difference cases, the mean displacement remains nearly unchanged, indicating that the mean response is mainly governed by the offset-induced thrust moment. In contrast, in the aeroelastic speed-mismatch cases, the equilibrium shift also varies with $\Delta\Omega$, showing that the aerodynamic coupling can make the mean displacement sensitive to the excitation-frequency condition.

3.5 Campbell Diagram

To the objective to analyze the impact of the mismatch speed in the harmonic behavior of the structure, It was made a Campbell Diagram considering the mismatch rotate speeds. For the present analyses the difference of speed $\Delta\Omega$ is always 10% of the standard speed, and is evaluate the in a superior and inferior cases. In addition, two ranges of velocities is made in the analyses, the first it is presented in Fig.17 that represents the range of operational speed, the second is presented in Fig.18 that has a bigger range, and the goal is to obtain more information about the effects that this mismatch can cause in the structure.

In Fig.17 is seen that the difference of the velocities almost does not affect the natural frequencies in this range. Within the operational range, the mismatch produces only small changes in most natural frequencies, indicating that the wing-dominated modes are weakly affected by the considered speed variation. The modes more directly associated with the propeller pitch and yaw degrees of freedom are more sensitive to the rotational speed, which is consistent with the gyroscopic coupling introduced by the rotating assemblies.

If we increase the range, as show in Fig.18, it can be seen that others frequencies related with the wing is also affected. This indicates that the influence of mismatch becomes more relevant as the rotational speed increases. Therefore, although the operational range shows limited modal sensitivity, the extended Campbell diagram suggests that speed mismatch may become important for higher-speed operating conditions or for configurations with stronger propeller-wing coupling.

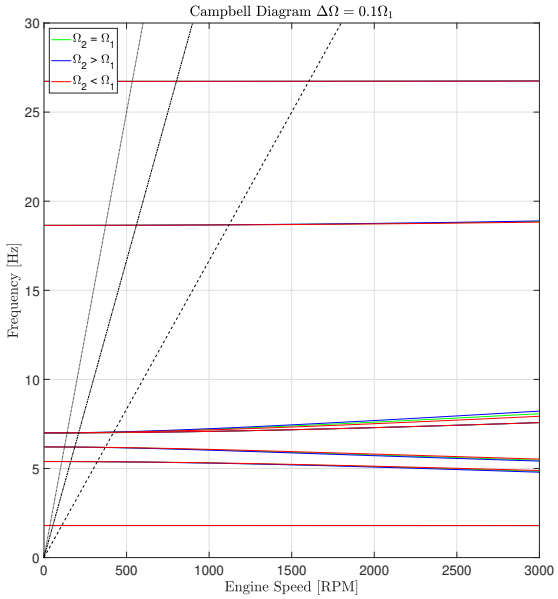


Figure 17 – Campbell Diagram for $\Delta\Omega = 0.1 \cdot \Omega_1$

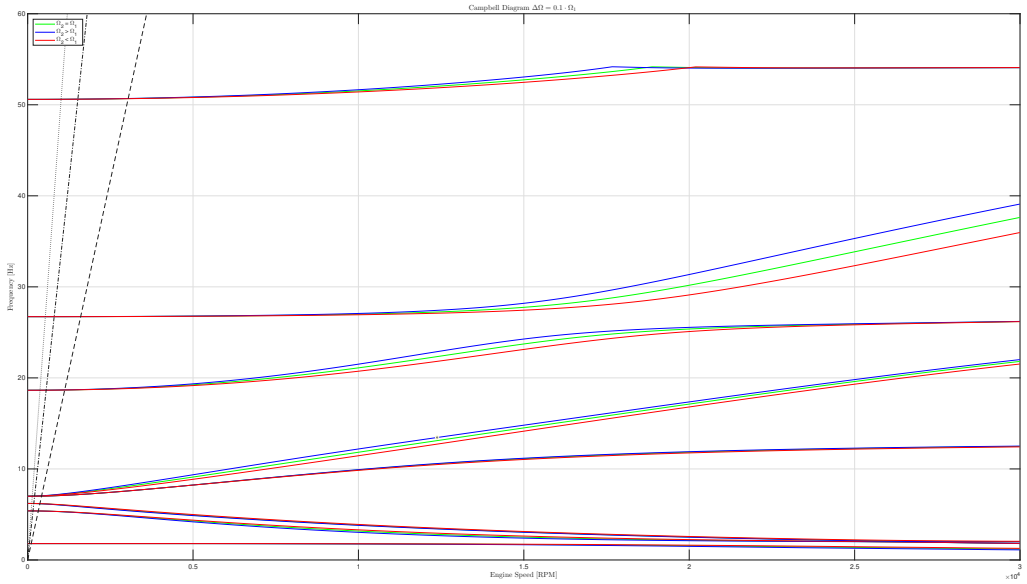


Figure 18 – Campbell Diagram for $\Delta\Omega = 0.1 \cdot \Omega_1$

4. Conclusion

This work investigated the vibration response of a flexible wing equipped with two electric motor-propeller assemblies subjected to mass-unbalance excitation. The proposed formulation included the bending and torsional motion of the wing, the pitch and yaw motion of the propeller assemblies, gyroscopic effects, thrust loads, unsteady aerodynamic loads, and a vertical offset between the wing elastic axis and the propeller axis. The aerodynamic model was coupled to the structural system through Wagner's approximation, allowing the comparison between purely structural and aeroelastic transient responses.

The results showed that small mismatches between the propeller rotational speeds generate a clear beating pattern in the wing-tip displacement response. This behavior is caused by the superposition of unbalance forces acting at slightly different excitation frequencies. As the speed mismatch decreases, the modulation period of the response increases, making the beating envelope more evident. The response also depends on which propeller is subjected to the speed variation, indicating that the spanwise location of the excitation affects the modal participation of the coupled wing-propeller system.

The comparison between structural and aeroelastic simulations showed that aerodynamic coupling significantly modifies the transient and steady-state responses. For the operating condition analyzed in this work, the aeroelastic model did not lead to a uniform reduction of the oscillatory amplitudes. Therefore, the purely structural model should not be interpreted as a generally conservative estimate of the vibration level.

The phase difference between the unbalance forces was also shown to be an important parameter. Increasing the phase difference reduced the resultant generalized forcing acting on the measured wing response, leading to lower steady-state amplitudes. The smallest responses were obtained close to the anti-phase condition, although complete cancellation is not expected because the propellers are attached at different spanwise locations and excite the coupled modes differently.

The inclusion of a vertical offset between the wing elastic axis and the propeller axis had a significant effect on the response. In the structural and aeroelastic simulations, the offset increased the oscillatory displacement amplitudes due to the additional moment arm associated with the propeller forces. The offset also modified the mean displacement of the response, indicating a shift in the equilibrium position caused by the coupling between thrust, bending, torsion.

Finally, the Campbell diagram analysis showed that the propeller speed mismatch has a limited influence on most natural frequencies within the operational speed range, while modes more directly associated with the propeller degrees of freedom are more sensitive to the rotational-speed variation. Over a wider speed range, additional modal branches are affected, indicating that the influence of mismatch becomes more relevant as the propeller speed increases.

5. Acknowledgments

The authors acknowledge the São Paulo Research Foundation (FAPESP) for supporting their research work (grant #2021/11258-5 - Engineering Research Center for the Aerial Mobility of the Future). G. R. Dias thanks the Brazilian Ministry of Education (CAPES Foundation) for granting him a Master Scholarship. A. G. Heck is grateful to the National Council for Scientific and Technological Development of Brazil for granting him a Master Scholarship.

6. Copyright Statement

The authors confirm that they, and/or their company or organization, hold copyright on all of the original material included in this paper. The authors also confirm that they have obtained permission, from the copyright holder of any third party material included in this paper, to publish it as part of their paper. The authors confirm that they give permission, or have obtained permission from the copyright holder of this paper, for the publication and distribution of this paper as part of the ICAS proceedings or as individual off-prints from the proceedings.

References

[1] Amir S Gohardani, Georgios Doulgeris, and Riti Singh. Challenges of future aircraft propulsion: A review of distributed propulsion technology and its potential application for the all electric commercial aircraft. *Progress in Aerospace Sciences*, 47(5):369–391, 2011.

[2] Paul M Rothhaar, Patrick C Murphy, Barton J Bacon, Irene M Gregory, Jared A Grauer, Ronald C Busan, and Mark A Croom. Nasa langley distributed propulsion vtol tilt-wing aircraft testing, modeling, simulation, control, and flight test development. In *14th AIAA Aviation Technology, Integration, and Operations Conference*, page 2999, Atlanta, EUA, 2014.

[3] VQ Liu Xu. Propeller-wing whirl flutter: an analytical study. *Delft University of Technology*, 2020.

[4] N. Böhnisch, C. Braun, S. Koschel, and P. Marzocca. Whirl flutter for distributed propulsion systems on a flexible wing. *AIAA SciTech*, 2022.

[5] Samet T Dede, Ali Tatar, Djamel Rezgui, and Jonathan E Cooper. Aeroelastic analysis of distributed electric propulsion flexible wings. In *IFASD 2024*, The Hague, The Netherlands, 2024.

[6] M. R. Amoozgar, S. Irani, and G. A. Vio. Aeroelastic instability of a composite wing with a powered-engine. *Journal of Fluids and Structures*, 2012.

[7] Mohammadreza Amoozgar, Michael I Friswell, Seyed Ahmad Fazelzadeh, Hamed Haddad Khodaparast, Abbas Mazidi, and Jonathan E Cooper. Aeroelastic stability analysis of electric aircraft wings with distributed electric propulsors. *Aerospace*, 8(4):100, 2021.

[8] S. A. Fazelzadeh, A. Mazidi, and H. Kalantari. Bending-torsional flutter of wings with an attached mass subjected to a follower force. *Journal of Sound and Vibration*, 2009.

[9] P. Mardanpour, D. H. Hodges, R. Neuhart, and N. Graybeal. Engine placement effect on nonlinear trim and stability of flying wing aircraft. *Journal of Aircraft*, 2013.

[10] M. Amoozgar, M. Hall, G. Dimitriadis, and J. E. Cooper. The effect of thrust vectoring on aeroelastic stability of electric aircraft. In *AIAA SciTech*, 2024.

[11] A. S. Mirabbashi, A. Mazidi, and M. M. Jalili. Analytical and experimental flutter analysis of a typical wing section carrying a flexibly mounted unbalanced engine. *International Journal of Structural Stability and Dynamics*, 19(02):1950013, February 2019.

[12] Ehsan Zafari, Mohammad Mahdi Jalili, and Abbas Mazidi. Nonlinear forced vibration analysis of aircraft wings with rotating unbalanced mass of the propeller system. *Journal of the Brazilian Society of Mechanical Sciences and Engineering*, 42:1–21, 2020.

[13] Daniel J Inman. *Vibration with control*. John Wiley & Sons, 2017.

[14] Fabrizio Nicolosi, Agostino De Marco, and Pierluigi Della Vecchia. Stability, flying qualities and longitudinal parameter estimation of a twin-engine cs-23 certified light aircraft. *Aerospace Science and Technology*, 24(1):226–240, 2013.